Aberration correction in 2D echocardiography

Svein-Erik Måsøy[1,2]^, Bastien Dénarié[2], Anders Sørnes[2], Espen Holte[1,3], Bjørnar Grenne[1,3], Torvald Espeland[1,3], Erik Andreas Rye Berg[1,3], Ole Marius Hoel Rindal[4], Wayne Rigby[5], Tore Bjåstad[2]

[1]Department of Circulation and Medical Imaging, Norwegian University of Science and Technology, Trondheim, Norway; [2]GE Vingmed Ultrasound AS, Horten, Norway; [3]St. Olavs hospital, Trondheim University Hospital, Trondheim, Norway; [4]Department of Informatics, University of Oslo, Oslo, Norway; [5]GE Research, Niskayuna, NY, USA

Contributions: (I) Conception and design: All authors; (II) Administrative support: All authors; (III) Provision of study materials or patients: All authors; (IV) Collection and assembly of data: SE Måsøy, EAR Berg, T Espeland, B Grenne, E Holte; (V) Data analysis and interpretation: All authors; (VI) Manuscript writing: All authors; (VII) Final approval of manuscript: All authors.

Correspondence to: Svein-Erik Måsøy, PhD. Department of Circulation and Medical Imaging, Norwegian University of Science and Technology, Postboks 8905, 7491 Trondheim, Norway. Email: svein-erik.masoy@ntnu.no.

Background: An aberration correction algorithm has been implemented and demonstrated in an echocardiographic clinical trial using two-dimensional (2D) imaging. The method estimates and compensates arrival time errors between different sub-aperture processor (SAP) signals in a matrix array probe.

Methods: Five standard views of channel data cineloops were recorded from 22 patients (11 male and 11 female) resulting in a total of 116 cineloops. The channel data were processed with and without the aberration correction algorithm, allowing for side-by-side comparison of images processed from the same channel data cineloops.

Results: The aberration correction algorithm improved image quality, as quantified by a coherence metric, in all 7,380 processed frames. In a blinded and left-right-randomized side-by-side evaluation, four cardiologists (two experienced and two in training) preferred the aberration corrected cineloops in 97% of the cases. The clinicians reported that the corrected cineloops appeared sharper with better contrast and less noise. Many structures like valve leaflets, chordae, endocardium, and endocardial borders appeared narrower and more clearly defined in the aberration corrected images. An important finding is that aberration correction improves contrast between the endocardium and ventricle cavities for every processed image. The gain difference was confirmed by the cardiologists in their feedback and quantified with a median global gain difference estimate between the aberration-corrected and non-corrected images of 1.2 dB.

Conclusions: The study shows the potential value of aberration correction in clinical echocardiography. Systematic improvement of images acquired with state-of-art equipment was observed both with quantitative metrics of image quality and clinician preference.

Keywords: Ultrasound; aberration correction; speed of sound variations; beamforming; echocardiography

^ ORCID: 0000-0001-9065-622X.

4604

Måsøy et al. Aberration correction in 2D echocardiography

Introduction

In medical ultrasound image reconstruction, the speed of sound in tissue is a vital parameter for image quality. The industry standard for tissue speed of sound in pulse-echo ultrasound systems is 1,540 m/s. This represents an average value over different tissue types (1) and is used for all patients in most systems. Some commercial systems allow the user to manually choose a sound speed or can automatically change it for improved image reconstruction.

State-of-the-art ultrasound probes contain arrays of hundreds [two-dimensional (2D) imaging probes] or thousands of elements [three-dimensional (3D) imaging probes]. The first step in array-based image reconstruction is focusing, that is, aligning across the array elements the received ultrasound wave emanating from a point in the body. The wave arrives at each element at different times because the propagation lengths are different and, potentially, because the propagation speed along each path is different. If these arrival time differences are removed correctly, the coherence sum over all elements of the time-delayed wave provides a strong signal from a given point. If the speed of sound in the medium is constant and known, the arrival time differences are calculated correctly, and this focusing results in high resolution and contrast when the process is repeated for all spatially sampled points in an image. Assuming an erroneous constant speed of sound will degrade image quality (2,3).

However, it is well known that different tissue types have different sound speeds (1,4,5). This leads to arrival-time errors over the array elements when a constant speed of sound is assumed during focusing. The arrival-time errors, or aberrations, degrade image quality (both resolution and contrast) due to a lowered coherence in the element summation process. Aberrations also affect the transmitted ultrasound wave, yielding a less focused ultrasound beam with a wider mainlobe and increased sidelobe level (6). The process of correcting for arrival time errors (and potentially amplitude variations) caused by heterogeneous tissue on receive, or both transmit and receive, is known as aberration correction.

Large local variations of the speed of sound are typically found in the body wall, which consists of the skin, subcutaneous fat, connective tissue, and interleaved muscle and fat layers with different sound speeds: 1,478 m/s in fat, 1,547 m/s in muscle, and 1,613 m/s in connective tissue (7).

A series of studies using excised human tissue have characterized aberrations generated by the abdominal wall (7-10), the breast (11), and chest wall (12). The severity of the aberration varies with the different body wall types and is correlated with the layer thickness (12). In the chest wall, aberrations are increased by interaction of the ultrasound field with the ribs and depends on the intercostal spacing (12).

Obesity, which increases the body wall thickness, leads to a significant reduction in images rated as "good" and an increase in those rated as "poor" (13). It also leads to increased use of more expensive, and more invasive, contrast-enhanced ultrasound (CEUS) and trans-esophageal echocardiography (TEE) to improve assessment of heart function (14).

Research into methods for compensating aberrations in pulse-echo imaging began more than 40 years ago. A selection of papers is provided in refs. (15-29). Many of these methods have been tested in lab settings or on a few selected clinical images but have never been implemented real-time on a clinical commercial system or validated in clinical trials with many patients.

In 2000, Rigby *et al.* (30) demonstrated real-time aberration correction in abdominal imaging in 13 healthy males using a multi-row abdominal probe. The results showed small but significant image improvements, such as improved visibility and contrast of known abdominal structures, reduced clutter in blood vessels, and improved brightness of liver tissue.

As a continuation of this work, the aberration correction algorithm described in ref. (30), called Adapt, has been modified and implemented to run in real-time on a GE Vivid E95 ultrasound system (GE Vingmed Ultrasound AS, Horten, Norway) by GE HealthCare and researchers at the Norwegian University of Science and Technology (Trondheim, Norway). The Vivid E95 system has a software beamforming platform (cSound), meaning that all beamforming and image processing is implemented in software using central processing units (CPUs) and graphics processing units (GPUs). The computing power of cSound allows for implementation of Adapt at imaging rates of more than 150 frames per second using factory settings for adult cardiac scanning sectors.

This study evaluates image quality improvements with the Adapt aberration correction algorithm in a 2D transthoracic echocardiography (TTE) clinical trial with 22 patients from the St. Olavs hospital, Trondheim University Hospital (Trondheim, Norway). Ultrasound channel data were recorded and then post-processed with and without Adapt. This allowed for a side-by-side comparison of images processed from the same channel data cineloops. A

coherence metric was developed to quantify image quality improvement using Adapt. This metric is compared with subjective image quality evaluations by four clinicians.

Methods

Adapt aberration correction algorithm

The aberration correction algorithm is implemented using channel data acquired with the 4Vc-D matrix array probe (GE Vingmed Ultrasound AS, Horten, Norway). It can be used in both fundamental and second-harmonic imaging modes. This probe has a sub-aperture processor (SAP) structure, where several thousand element signals are pre-beamformed in sub-aperture groups into 192 channel signals distributed over the array aperture. The Vivid E95 system can store ultrasound data from each SAP in the 4Vc-D probe prior to beamforming. Such data are here referred to as channel data. In this study, the Adapt algorithm is applied off-line to the captured channel data.

Like the earlier work (30), the algorithm estimates and removes arrival time errors from the channel signals. The arrival time of each channel signal, after beamforming time-delays have been applied, is calculated with respect to a common reference signal, the beamsum, the sum of the time-delayed channel signals, using the normalized complex "correlation sum",

$$C_i(\theta) \equiv \frac{\Sigma_r s_i(r,\theta) B^*(r,\theta)}{\sqrt{\Sigma_r |s_i(r,\theta)|^2 |B(r,\theta)|^2}} \qquad [1]$$

where $s_i(r, \theta)$ is the ith baseband channel signal, a function of range sample r and receive direction θ, $B^*(r,\theta) = \sum_{i=1}^{N} s_i^*(r,\theta)$ is the complex conjugate of the beamsum signal, and N is the total number of channel signals. The phase of a speckle-like signal is a random variable uniformly distributed over $\pm\pi$; the sum over range samples averages over this random phase leaving the mean phase difference, which is proportional to the relative time delay between the channel and beamsum signals,

$$\tau_i = (2\pi f)^{-1} \text{Phase}\{C_i(\theta) * F(\theta)\} \qquad [2]$$

where the correlation sums are filtered over receive directions θ, $F(\theta)$ is a convolution filter kernel function, and f is the nominal center frequency of the beamsum signal. This filtering adds additional averaging provided the arrival time errors vary slowly over the filter length.

Unlike the earlier work, however, the arrival time errors τ_i are applied as corrections only to the receive beamforming time delays and not to both the transmit and receive beamforming time delays. This avoids potential ultrasound power regulatory issues, since the transmit beamforming isn't modified. It also allows comparison of Adapt-corrected and uncorrected images created using the same channel data.

Data collection and processing

Twenty-two patients (11 women and 11 men) were recruited over 3 working days in the Clinic of Cardiology at St. Olavs hospital during the autumn of 2020. The patients had a minimum, median, and maximum age of 54, 72, and 86 years respectively. The different recording days represented normal days in the clinic. Inclusion criteria were simply the willingness to participate in the study, age above 18 years, and a clinical indication for a TTE. Exclusion criteria were hemodynamically unstable patients, patients with arrhythmia, or lack of competent consent. The study was conducted in accordance with the Declaration of Helsinki (as revised in 2013). The study was approved by the Regional Committee for Medical and Health Research Ethics of Mid-Norway (No. 142295), and all patients provided written consent.

For each patient, at least one cineloop containing at least one heart cycle was recorded for the five standard 2D views: parasternal long axis (PLAX), parasternal short axis (PSAX), apical four chamber (A4C), apical two chamber (A2C), and apical long axis (ALAX). Some patients had several recordings of the same cardiac view, and for some patients fewer than five views were recorded due to technical difficulties in the clinic. Also, in one case only 20 frames (the standard number of frames per cineloop was 64) were recorded due to a technical issue with the channel data recording procedure. This cineloop was still included in the image quality assessment by the clinicians.

Default Vivid E95 factory settings for the 4Vc-D probe were used with the Cardiac_E application (second-harmonic imaging mode). All data were recorded by two senior cardiologists (BG and EH) with 7 and 11 years of experience as consultant cardiologists. A machine learning classifier developed by Østvik et al. (31) was used to automatically label the cardiac view. This classifier has a reported accuracy of 98.9±0.6.

The recorded data were post-processed using a stand-alone workstation computer running a version of the Vivid E95 cSound beamforming and image processing software implemented in MATLAB (The Mathworks, Inc.,

Figure 1 Image processing chain for Adapt (name of aberration correction algorithm) images. For the standard images, the Adapt and gain compensation sections were omitted. DICOM, Digital Imaging and Communications in Medicine.

Natick, MA, USA). This code does not have European Union Conformité Européene (CE) or US Food and Drug Administration (FDA) approval. It implements all state-of-the-art image reconstruction and post-processing steps normally performed on the Vivid E95 system. Each channel data cineloop was processed in two different ways:

(I)   Standard cSound processing, yielding conventional images as displayed by the E95 system during real-time scanning (standard images);

(II) Aberration correction inserted into the cSound processing, yielding aberration corrected images (Adapt images).

All other processing steps were identical except for the global gain adjustment described in the next section. This allowed for side-by-side comparison of images processed with and without aberration correction from the same channel data cineloops. A total of 116 cineloops were recorded and processed to a Digital Imaging and Communications in Medicine (DICOM) format for display and clinical evaluation in EchoPAC (GE Vingmed Ultrasound AS, Horten, Norway), a stand-alone image evaluation and analysis software package provided with the Vivid E95 system.

Gain compensation

The aberration correction algorithm typically increases the signal intensity of the cardiac tissue since it improves the focusing algorithm. This leads to a systematic gain increase in the aberration corrected images, which was compensated for the images to appear equalized with respect to global gain settings. The display gain for the aberration corrected images was reduced algorithmically to minimize the difference in intensity with the corresponding standard image. The difference in intensity of the 20% brightest pixels between the aberration corrected and standard image was averaged over all 64 frames and used as a global gain reduction for the Adapt images. After this compensation, the images appeared to have similar global gain. The total image processing chain is presented in *Figure 1*.

Image quality parameter

Image quality improvement was quantified in two ways.

First, an image quality metric based on signal coherence was developed. The coherence factor (CF) (32,33), the ratio between the coherent and incoherent sums over the channel signals $s_i(r, \theta)$,

$$\mathrm{CF}(r,\theta) \equiv \frac{\left|\sum_{i=1}^N s_i(r,\theta)\right|^2}{N \sum_{i=1}^N \left|s_i(r,\theta)\right|^2} \qquad [3]$$

using the notation from the "Adapt aberration correction algorithm" section. The CF yields a normalized ultrasound image with values ranging from zero to one; it is a measure of the similarity of time-delayed channel signals. A value of one indicates identical, time-aligned signals (fully correlated). CF decreases as arrival-time errors increases. A similar decrease occurs for speckle-like reflectors, for which the channel signals are no longer identical. The global image coherence (GIC) is

$$\mathrm{GIC} = \frac{\sum_{\theta=-\theta_0}^{\theta_0} \sum_{r=R_0}^R \left|\sum_{i=1}^N s_i(r,\theta)\right|^2}{\sum_{\theta=-\theta_0}^{\theta_0} \sum_{r=R_0}^R \sum_{i=1}^N \left|s_i(r,\theta)\right|^2} \qquad [4]$$

The GIC averages the coherent and incoherent sums over all receive directions $-\theta_0 \leq \theta \leq \theta_0$ and range samples $R_0 \leq r \leq R$ in an image frame, where $2\theta_0$ is the scanning sector opening angle and R is the total number of range samples. In this work $R_0 = R/3$ to avoid any near-field reverberations. The GIC can also be averaged over all frames in a cineloop, called the average GIC. Since GIC estimates errors in focusing, it is plausible to assume that it correlates with image quality (but not necessarily linearly).

Second, image quality improvement was evaluated by four clinicians, two senior cardiologists (BG and EH), and two fellows in cardiology (TE and EARB) with 10 years of experience with echocardiography. Images with and without aberration correction were displayed side-by-side in EchoPAC but randomized left and right for each recording. Since both the aberration corrected and uncorrected (standard) images were created from the same channel data, they were displayed with frame synchronization. Thus, the synchronized cineloops could be paused, and individual
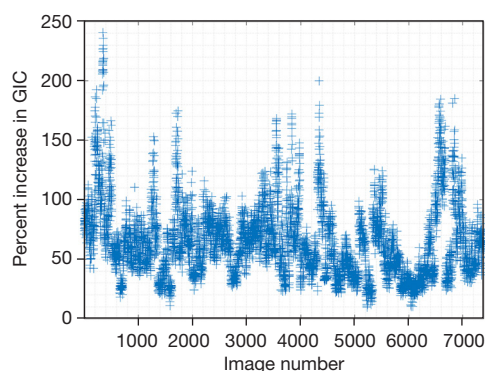
Figure 2 Percentage increase in GIC after aberration correction for all 7,380 processed frames. GIC, global image coherence.

Table 1 Preferred cineloop in randomized side-by-side comparison for each clinician

Clinician	Standard	Adapt	Equal
1	0	116	0
2	4	111	1
3	0	116	0
4	7	109	0
Sum	11	452	1
Percentage	2.4	97.4	0.2

The "Adapt" column refers to the aberration corrected cineloop.

frames could be compared.

The clinicians were instructed to select the preferred processing for each paired cineloop or to judge them equally preferable. The protocol stated the clinicians could reduce the replay speed of the paired cineloops or freeze the cineloops and step through at most 10 consecutive paired frames. They could also adjust a display gain which was applied equally to both sides of the paired cineloops. No specific image quality criteria were defined or agreed upon in advance. All the clinicians were made aware of the principles of aberration correction and that it may potentially improve the images.

Results

Figure 2 shows the change in the GIC after aberration correction from all frames and all subjects. Note that GIC increases with aberration correction for every processed frame.

Table 1 presents the results of the clinicians' preference

for cineloops. The clinicians preferred the aberration corrected cineloop 97% of the time. Two of the clinicians (one experienced and one fellowed) preferred the aberration corrected cineloop in all 116 cineloops; the other two preferred the standard processing in 11 (of 116) cineloops. One cineloop pair was rated of equal quality by one clinician.

Figure 3 shows average GIC (GIC averaged over all frames in one cineloop) for the standard images and the aberration corrected images, together with the percentage increase in average GIC after aberration correction and the gain compensation value applied to all cineloops. The horizontal axis displays the patient number and cardiac view. The legend refers to the numbering of the image case examples presented later in this section. The dotted line in each plot indicates the median value of each parameter.

The median percentage increase in the average GIC after aberration correction is 62%, and the median value of the applied gain compensation is 1.2 dB. The Pearson linear correlation coefficient between the average GIC ratio increase and the gain compensation is 0.67.

The GIC parameter calculated for all frames are sorted by view in *Figure 4* using boxplots. Using a two-sided Wilcoxon rank-sum test all views obtain a statistically significant increase ($P<0.05$) in GIC with Adapt. A significant difference ($P<0.05$) between the parasternal and apical views before and after aberration correction is also observed. The parasternal short-axis view has the lowest observed GIC values in both instances.

In *Figure 5* (*Videos 1,2*) and *Figure 6* (*Videos 3-5*), a selected frame from all 5 recordings of patient 10 are presented.

These images are here referred to as case example 1 (see *Figure 3*). The standard image is displayed on the left and the aberration corrected image on the right. Aberration correction clearly improved all the images from this patient. In general, image contrast and sharpness is improved. The cardiac structures, in particular, the endocardial borders and valves, appear thinner and more clearly defined. This is clearly visible in the ALAX view (*Figure 6C*, bottom row) from this patient, where the mitral valve leaflets and endocardial borders become very clear after aberration correction.

In the following, selected case examples are presented. The numbering corresponds to the legend of *Figure 3*.

Selected frames for case examples 2 (*Video 6*), 3 (*Video 7*), and 7 (*Video 11*) are presented in *Figure 7*. These three cases are the ones with the largest increase in the average GIC
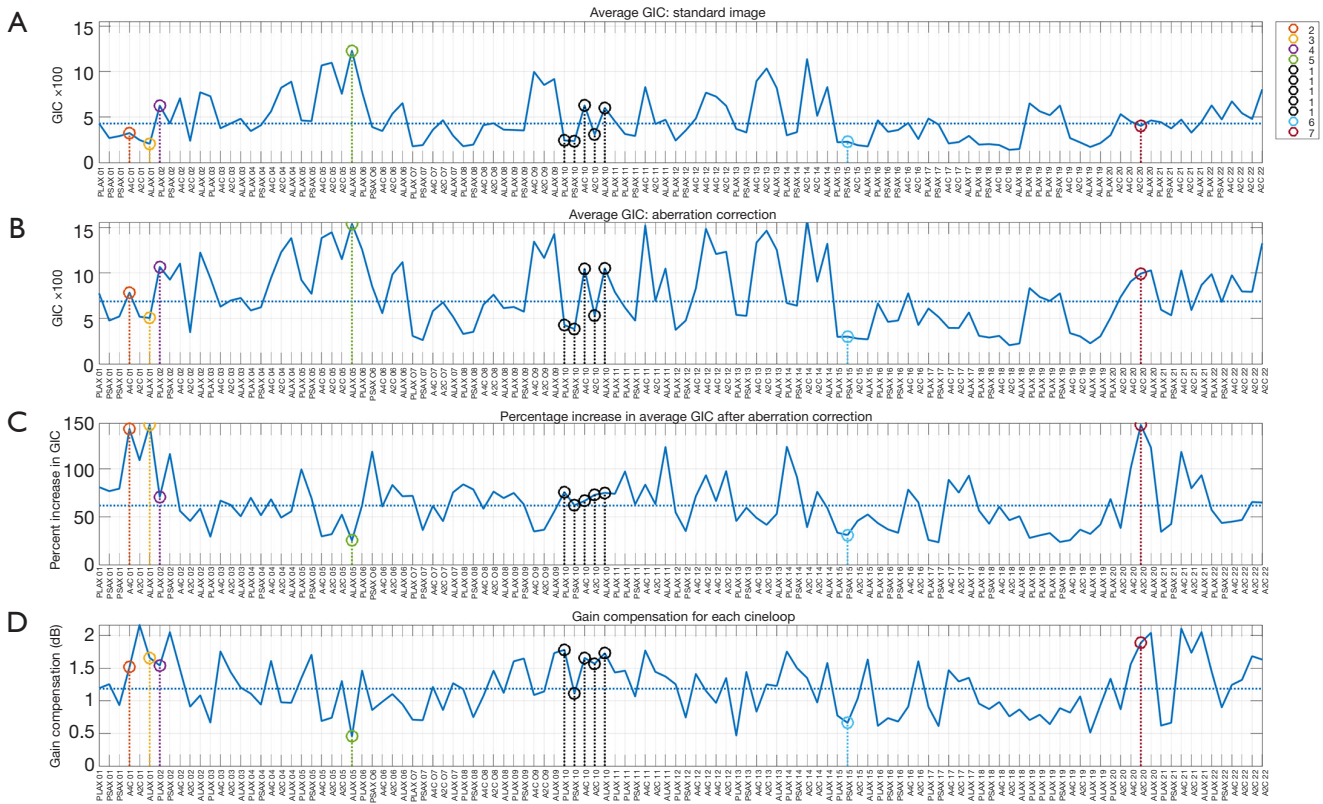
Figure 3 Average GIC values and gain compensation over all frames in each recorded cineloop. (A) Average GIC before aberration correction. (B) Average GIC after aberration correction. (C) The percentage increase in the average GIC parameter after aberration correction. (D) Calculated gain compensation value for each cineloop. The dotted line in each plot indicates the median value of each parameter. The X-axis shows the patient number and cardiac view. The legend refers to the numbering of the image case examples presented later in this section. The coloring of the circles in the legend refers to different patient cases. The black colored cases indicate that all are from the same patient (patient 10), presented with images as case example 1 below. GIC, global image coherence; PLAX, parasternal long axis; PSAX, parasternal short axis; A4C, apical four chamber; A2C, apical two chamber; ALAX, apical long axis.
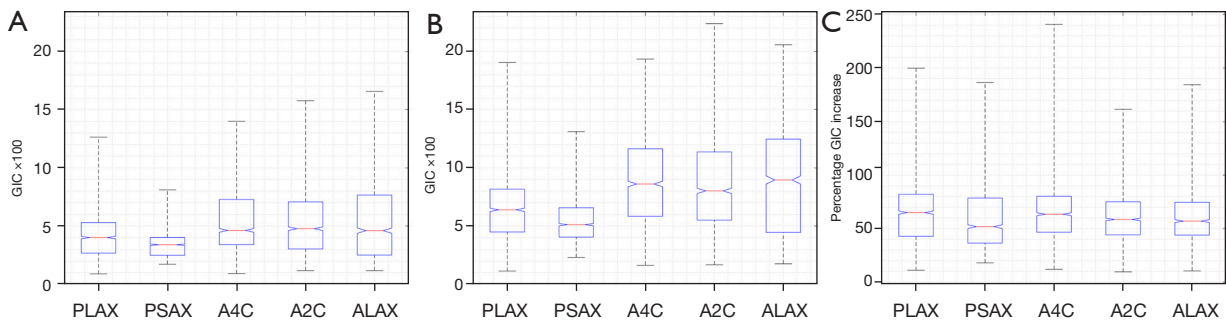
Figure 4 Boxplots of GIC as a function of image view. On each box, the central mark (red line) indicates the median, and the bottom and top edges of the box indicate the 25th and 75th percentiles, respectively. The whiskers extend to the most extreme data points not considered outliers. The notches indicate the 95% confidence interval of the median value, meaning that the if the notches in the box plots do not overlap, it is possible to conclude with 95% confidence that the true medians differ. (A) GIC without Adapt. (B) GIC with Adapt. (C) Percentage increase in GIC after aberration correction as a function of cardiac view. GIC, global image coherence; PLAX, parasternal long axis; PSAX, parasternal short axis; A4C, apical four chamber; A2C, apical two chamber; ALAX, apical long axis.
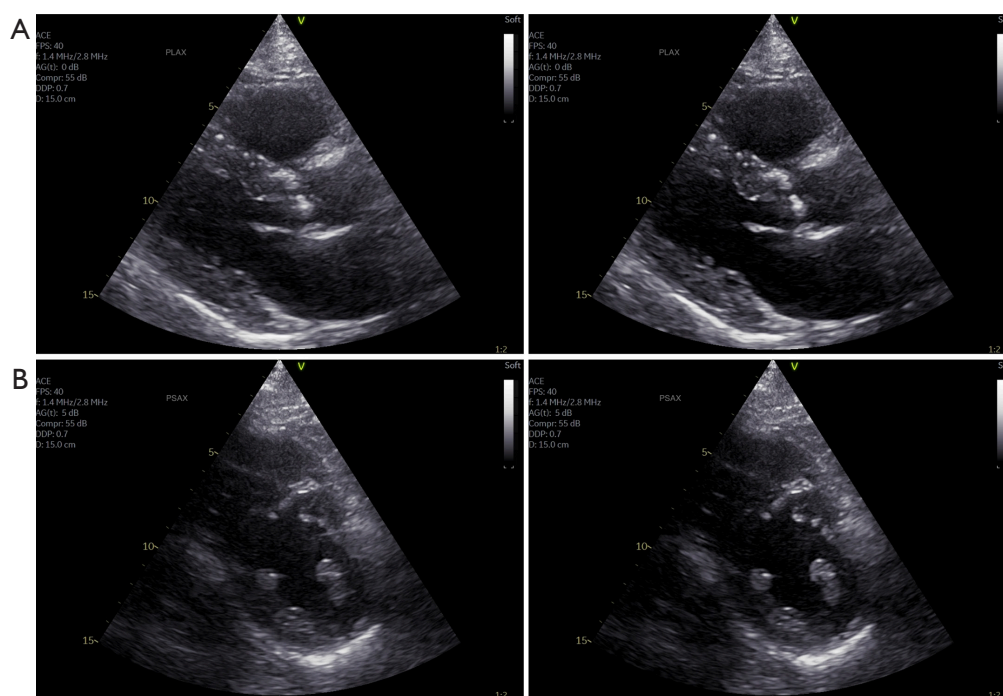
Figure 5 Case example 1. Parasternal views from patient 10. Standard image to the left and aberration corrected image to the right. (A) Top row: PLAX view (*Video 1*). (B) Bottom row: PSAX views (*Video 2*). PLAX, parasternal long axis; PSAX, parasternal short axis.

parameter after aberration correction. Note also that these cases have an GIC value around the median value of all images.

In case examples 2 and 3, the septal wall is almost not visible before aberration correction is applied. The images appear noisy prior to aberration correction, and there is a significant reduction of noise in the cavity as the signal intensity from the tissue is increased after aberration correction. Endocardial borders and valves are sharpened with a generally improved contrast with respect to the cavity.

Selected frames from case examples 4 (*Video 8*), 5 (*Video 9*), and 6 (*Video 10*) are presented in *Figure 8*. The average GIC for case example 4 is above the median before correction; the GIC improvement with correction is near the median improvement. Case examples 5 and 6 have the highest and close to lowest GIC value, and both obtain some of the lowest increases in average GIC after aberration correction. These numbers match well with the observed image quality and improvement after aberration correction in the displayed images. Still, the same trend is also visible here as for the other presented case examples with improved image contrast, endocardial borders, and sharper structures (although very moderate improvements for case 5, but quite

clear around the valve and the thin portion of the right ventricle visible in the upper right part of the image).

Discussion

The aberration correction algorithm is shown to increase the GIC, a metric of beamforming time-delay accuracy. The clinicians reported that the aberration corrected images appeared sharper with better contrast and less noise. The corrected image was preferred in a blind comparison in 97% of the cases. Structures such as valve leaflets, chordae, and the endocardium appear narrower and more clearly defined in the aberration corrected images. In many examinations, the improvement was visible in the cineloops running at full speed. In a few of the cases, the improvements were apparent only at reduced replay speed or in still frames. In a few cases (in still frames), the clinicians reported that some parts of the image were improved while other parts were slightly degraded. The slight degradation was not deemed to be of clinical significance. The algorithm was reported to be stable with no visible image artefacts in replay mode.

The image quality improvement, as measured by the GIC, varied by patient. This is expected. It is well-known that image quality varies by patient, so that the maximum
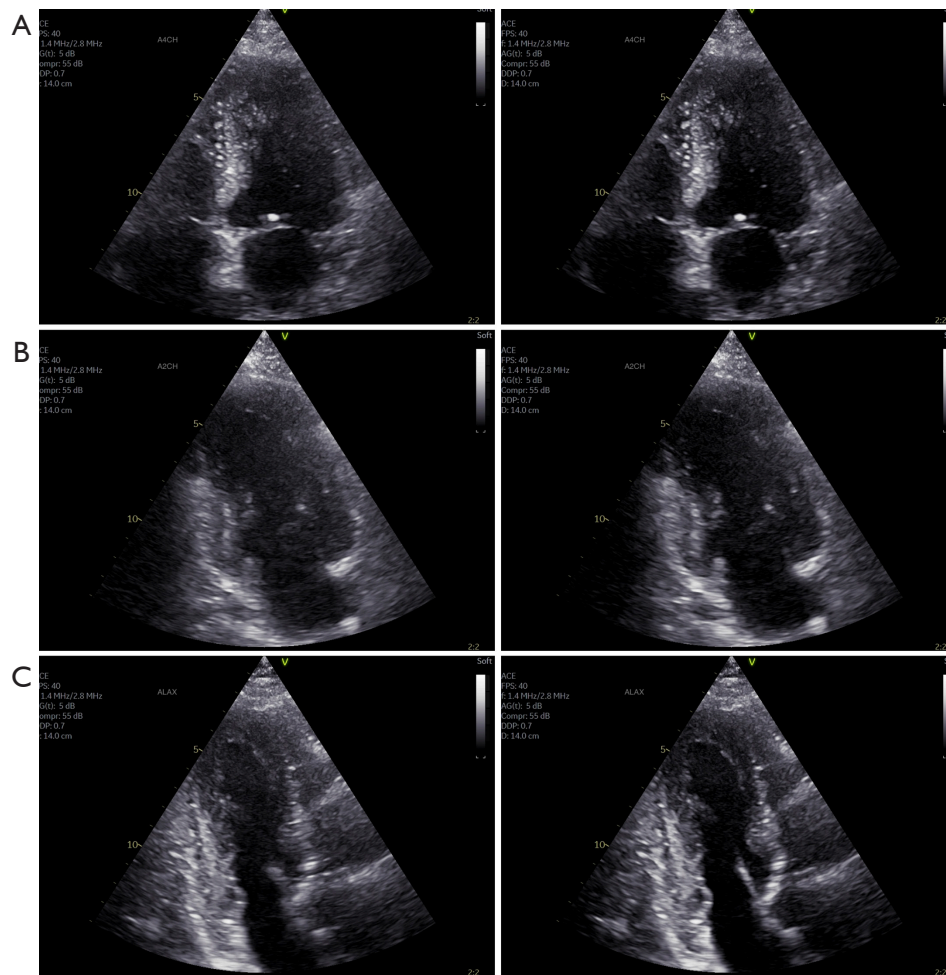
Figure 6 Case example 1. Apical views from patient 10. Standard image to the left and aberration corrected image to the right. The rows display (from top to bottom): (A) A4C view (*Video 3*); (B) A2C view (*Video 4*); (C) ALAX view (*Video 5*). A4C, apical four chamber; A2C, apical two chamber; ALAX, apical long axis.

image improvement is inherently patient-dependent. In addition, it is unlikely that adjusting beamforming time-delays can fully correct for all image degradation. As stated previously, the algorithm aims at compensating the effect of a variable speed of sound in the body wall. There are, however, several other acoustic effects degrading image quality in echocardiography, such as reverberations, scattering and shadowing from ribs, lung, and other structures. See, for example, Fatemi *et al.* (34). These effects are often accompanied by clutter (or haze) overlying some or all of the ultrasound image. In the examples presented here, while clutter is also visible after aberration correction in many cases, it is also significantly reduced due to the increase in tissue intensity from the correction.

The GIC parameter correlates well with clinicians' assessment of image quality: the GIC increased with aberration correction in every instance, and the clinicians preferred the aberration-corrected cineloop in 97% of the instances. This is particularly clear from case examples 5 and 6 (*Figure 8C-8F*) which represent the cases with the highest and one of the lowest average GIC parameter for all recorded cineloops. Sorted by view, the GIC increased (with statistical significance) using Adapt for all views. The PLAX and A4C view obtained the highest increase whereas the PSAX view obtained the smallest increase.

Two clinicians (one experienced and one in training) preferred the aberration correction algorithm for all the analyzed cineloops. In 11 cases (2.4% of total cases) two
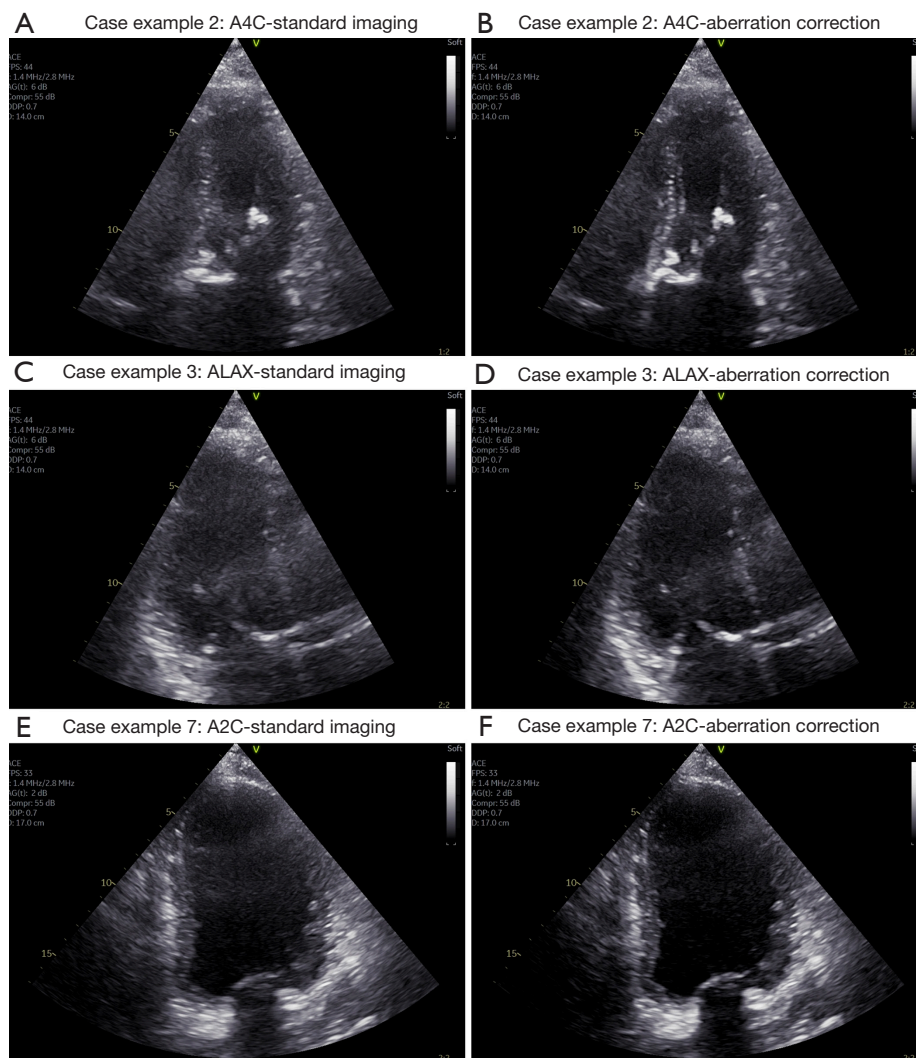
Figure 7 Case examples 2, 3, and 7. (A,B) Case example 2 (patient 1, *Video 6*). (C,D) Case example 3 (patient 1, *Video 7*). (E,F) Case example 7 (patient 20, *Video 11*) (see *Figure 2*). A4C, apical four chamber; A2C, apical two chamber; ALAX, apical long axis.

clinicians preferred the non-Adapt corrected image, but they only agreed on this in one instance. This means that in 115 of 116 cases (99%) 3 out of 4 clinicians preferred the Adapt corrected image. One clinician found one case (0.2%) to be of equal quality. It is not clear why the clinicians disagreed in these few instances. (They were not asked to review the results). Since no criteria were agreed upon for defining image quality, it may simply reflect differences in personal preferences.

The GIC parameter is based on the CF (33), which is almost identical to the focusing criterion defined by Mallart *et al.* (32), except for a range-averaging term. For a medium with delta-function spatial correlations, the

focusing criterion is shown to be independent of frequency and probe aperture size in the focal region of the probe (32). This assumption is not valid for coherent structures like the heart. The GIC parameter is calculated over a large image range, meaning it is evaluated also outside the probe transmit focal region. This renders the GIC dependent on image view. In principle, it is also dependent on the beamforming algorithm used by a specific system, meaning it is not straightforward to compare GIC values between systems or imaging modes. Still, for a given system, view dependent values of the GIC may be established and used qualitatively for evaluating image quality.

The gain increase generated by the aberration correction
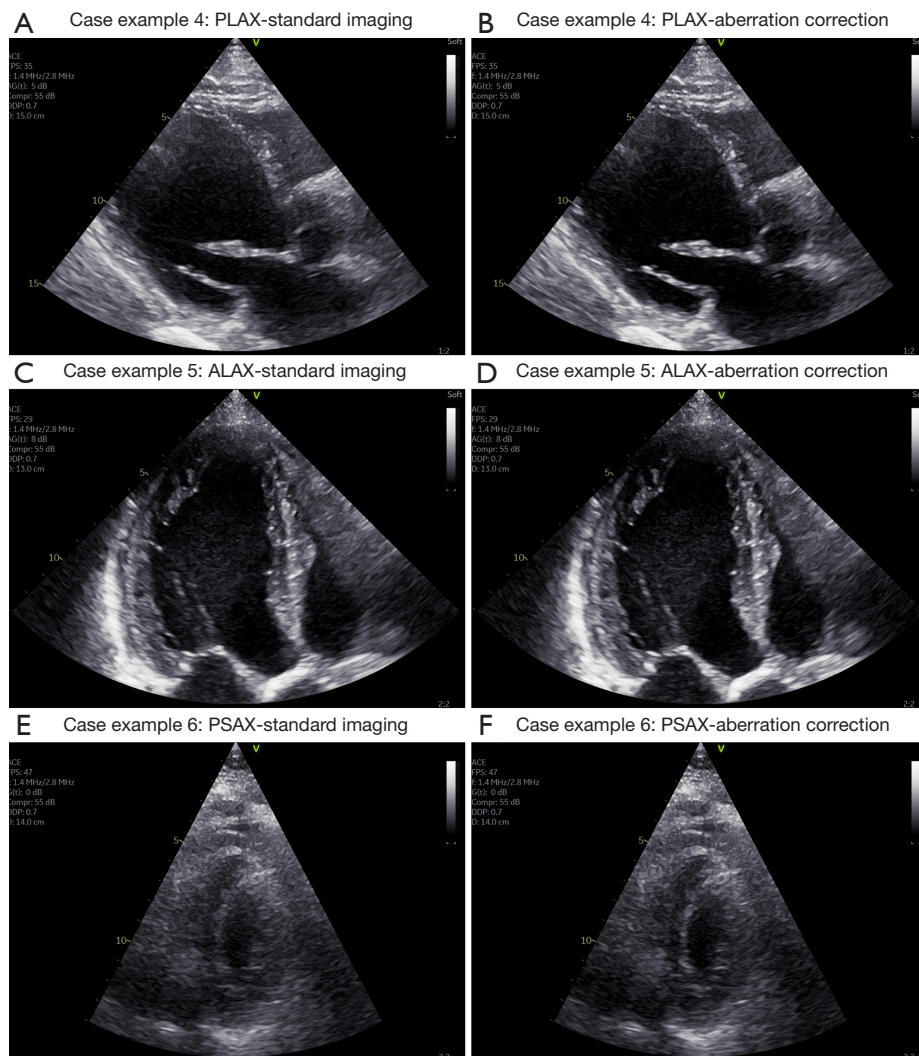
Figure 8 Case examples 4, 5, and 6. (A,B) Case example 4 (patient 2, *Video 8*). (C,D) Case example 5 (patient 5, *Video 9*). (E,F) Case example 6 (patient 15, *Video 10*) (see *Figure 2*). PLAX, parasternal long axis; PSAX, parasternal short axis; A4C, apical four chamber; A2C, apical two chamber; ALAX, apical long axis.

algorithm was removed to make it more difficult for the clinicians to observe which image had been processed with the algorithm. Randomizing the images to the left and right without gain compensation is fairly pointless, since the brighter cardiac structures in the Adapt images were easily detected by non-clinicians reviewing the images during testing of the evaluation procedure.

Three levels of pixel intensities were considered for the gain compensation method. Using 10% or 30% of the brightest pixels was also evaluated, but 20% was deemed to be a good compromise. In some cases, the chosen value could potentially reduce the gain a bit too much in the Adapt image, but in others too little. Overall, the method seemed to perform well as documented through case examples presented in this paper. The compensation varied between (0.5–2.2) dB, with a median value of 1.2 dB, a significant increase of tissue signal level after aberration correction.

Further technical improvements

The current implementation of the Adapt algorithm is applied on receive only. This avoids regulatory challenges to changing adaptively time-delays in an ultrasound system.
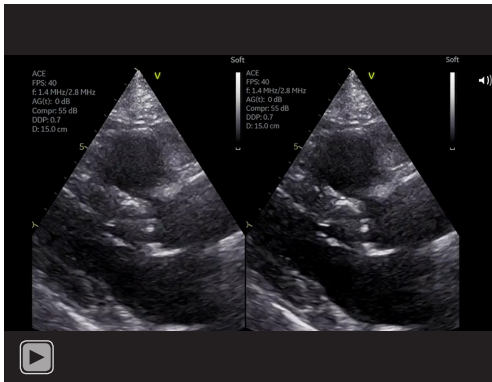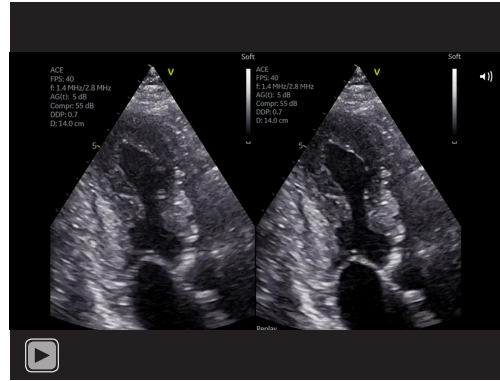
Video 1 Case example 1: parasternal long axis (PLAX) view. Left: no adapt; right: adapt.
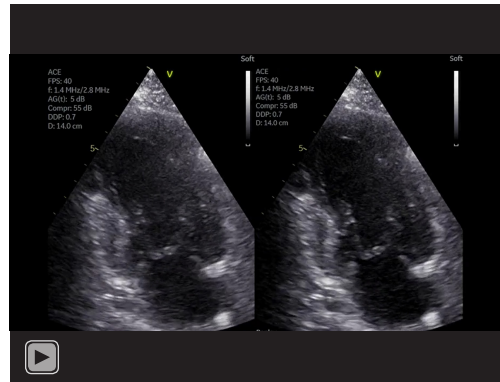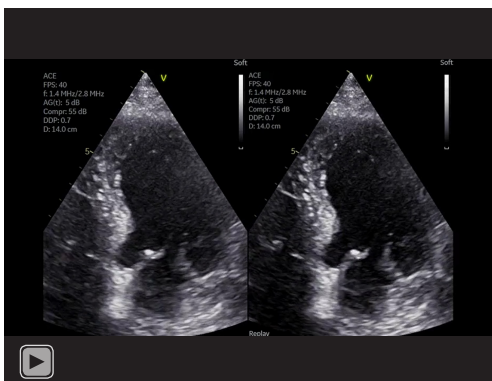

Video 4 Case example 1: apical two chamber (A2C) view. Left: no adapt; right: adapt.
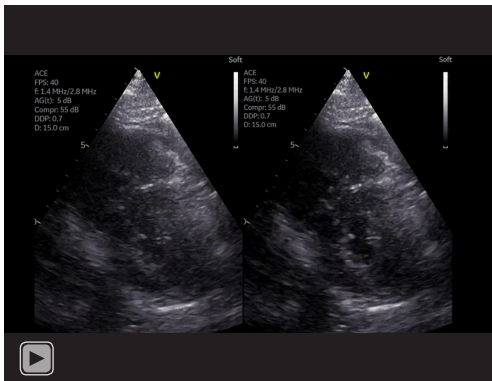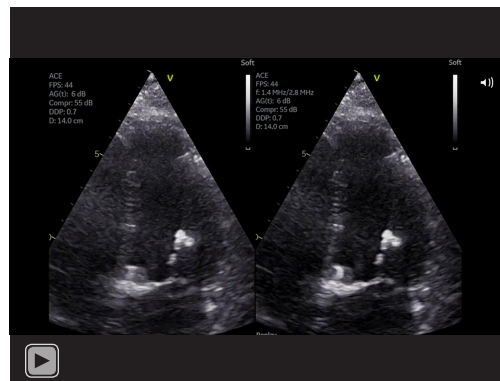

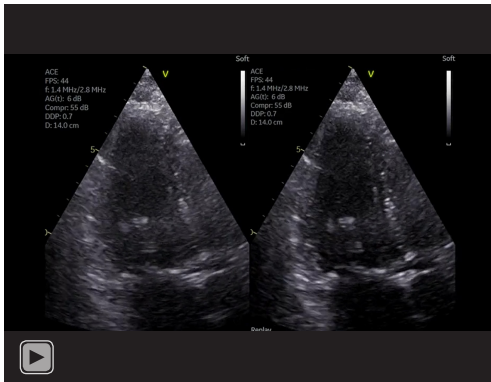**Video 2** Case example 1: parasternal short axis (PSAX) view. Left: no adapt; right: adapt.

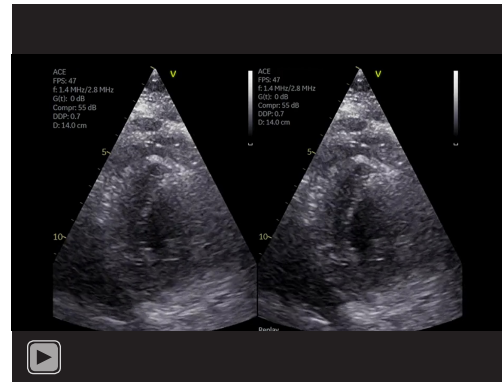**Video 5** Case example 1: apical long axis (ALAX) view. Left: no adapt; right: adapt.

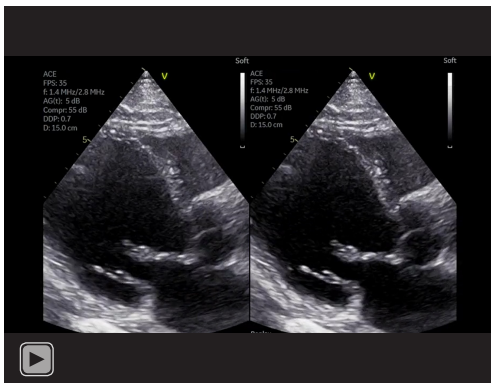**Video 3** Case example 1: apical four chamber (A4C) view. Left: no adapt; right: adapt.

Video 6 Case example 2: apical four chamber (A4C) view. Left: no adapt; right: adapt.
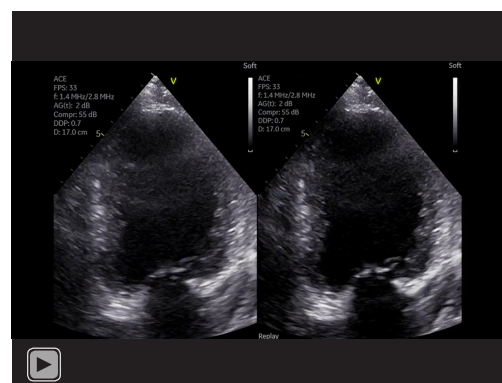
Video 7 Case example 3: apical long axis (ALAX) view. Left: no adapt; right: adapt.
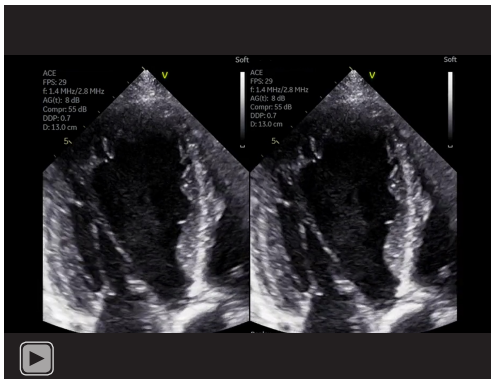

Video 10 Case example 6: parasternal short axis (PSAX) view. Left: no adapt; right: adapt.

Video 8 Case example 4: parasternal long axis (PLAX) view. Left: no adapt; right: adapt.

Video 11 Case example 7: apical two chamber (A2C) view. Left: no adapt; right: adapt.

In refs. (30,35) aberration correction was performed both on transmit and receive and was shown to improve image quality in phantoms and during *in-vivo* imaging. The benefit of transmit and receive correction has also been demonstrated in *in-vitro* and in-silico studies (25,36). This is a clear opportunity for future technical improvements using Adapt, but it would also require more research into how changing time-delays adaptively on transmit can modify the transmitted energy from an ultrasound system with respect to regulatory limitations.

Limitations

This study is limited in the number of patients examined

Video 9 Case example 5: apical long axis (ALAX) view. Left: no adapt; right: adapt.

and it is a single center study. A larger multi-center clinical trial with more clinicians evaluating the images would improve the strength of the study.

The gain compensation method was chosen based on subjective evaluation from the authors of this work who are engineers and was not subject to evaluation by the authors who are clinicians. This may have led to cineloops obtaining too large gain suppression, rendering them favorable to clinicians in appeared improved contrast.

The GIC parameter is based on coherence, a metric for measuring similarity of waveforms received by the ultrasound probe. The GIC increased after using Adapt, and the clinicians favored the images using Adapt, but this is not a clear indication that GIC can measure image quality. Further studies would be required to establish a clear relationship between the GIC and evaluation from clinicians.

Conclusions

This work shows that receive-only aberration correction is feasible and improves images in pulse-echo imaging of the heart. A coherence metric {the GIC Eq. [4]}, increased in all 7,380 processed images after applying aberration correction. Four clinicians selected the cineloop they preferred in a blinded and left-right-randomized side-by-side display of aberration-corrected and uncorrected images. The clinicians preferred the aberration corrected cineloops in nearly every case, in 97% of the 116 analyzed cineloops.

Aberration correction improved resolution and contrast in the images, yielding sharpened structures, thinner valves, cords, and improved endocardial border visualization. The improvement varied with patient and image view; the PLAX and A4C views obtained the largest improvements in GIC, and this was statistically significant. The PSAX view received the smallest improvement.

Perhaps the most significant effect of aberration correction is improved cardiac tissue intensity, improving contrast with the heart chambers in all images. The brightest image pixels increased by a median value of 1.2 dB calculated over all frames of the 116 cineloops. The gain increase was strongly correlated with the relative increase in average GIC in the aberration corrected images.

Aberration correction has here been shown to systematically improve clinical echocardiography images. The enhanced image quality may facilitate and improve clinical evaluation of echocardiograms and diagnosis of cardiac disease. Larger studies using Adapt are required to validate this hypothesis.

Footnote

Conflicts of Interest: All authors have completed the ICMJE uniform disclosure form (available at https://qims.amegroups.com/article/view/10.21037/qims-22-895/coif). SEM reports that in addition to being 100% employed by The Norwegian University of Science and Technology, he has had a 20% position in GE Vingmed Ultrasound AS since May 2nd 2022, which potentially benefits from documenting the medical benefits of adaptive imaging as implemented on their ultrasound systems. BD reports that he is paid a salary by GE HealthCare, which potentially benefits from documenting the medical benefits of adaptive imaging as implemented on their ultrasound imagers. AS reports that he is paid a salary by GE HealthCare, which potentially benefits from documenting the medical benefits of adaptive imaging as implemented on their ultrasound imagers. EARB report that he has received PhD funding from The Centre for Innovative Ultrasound Solutions, where GE Vingmed Ultrasound AS is one of 22 private and public funding partners. OMHR reports that he has received Post Doc funding from the Centre for Innovative Ultrasound Solutions, where GE Vingmed Ultrasound AS is one of 22 private and public funding partners. WR reports that he is paid a salary by GE, which potentially benefits from documenting the medical benefits of adaptive imaging as implemented on their ultrasound imagers. TB reports that he is paid a salary by GE HealthCare, which potentially benefits from documenting the medical benefits of adaptive imaging as implemented on their ultrasound imagers. The other authors have no conflicts of interest to declare.

Ethical Statement: The authors are accountable for all aspects of the work in ensuring that questions related to the accuracy or integrity of any part of the work are appropriately investigated and resolved. The study was conducted in accordance with the Declaration of Helsinki (as revised in 2013). The study was approved by the Regional Committee for Medical and Health Research Ethics of

Mid-Norway (No. 142295), and all patients provided written consent.

References

1. Ludwig GD. The velocity of sound through tissues and the acoustic impedance of tissues. J Acoust Soc Am 1950;22:862-6.
2. Anderson ME, Trahey GE. The direct estimation of sound speed using pulse-echo ultrasound. J Acoust Soc Am 1998;104:3099-106.
3. Chen Q, Zagzebski JA. Simulation study of effects of speed of sound and attenuation on ultrasound lateral resolution. Ultrasound Med Biol 2004;30:1297-306.
4. Goldman DE, Hueter TF. Tabular data of the velocity and absorption of high-frequency sound in mammalian tissues. J Acoust Soc Am 1956;28:35-7.
5. Goss SA, Johnston RL, Dunn F. Comprehensive compilation of empirical ultrasonic properties of mammalian tissues. J Acoust Soc Am 1978;64:423-57.
6. Måsøy SE, Johansen TF, Angelsen B. Correction of ultrasonic wave aberration with a time delay and amplitude filter. J Acoust Soc Am 2003;113:2009-20.
7. Mast TD, Hinkelman LM, Orr MJ, Sparrow VW, Waag RC. Simulation of ultrasonic pulse propagation through the abdominal wall. J Acoust Soc Am 1997;102:1177-90.
8. Hinkelman LM, Liu DL, Metlay LA, Waag RC. Measurements of ultrasonic pulse arrival time and energy level variations produced by propagation through abdominal wall. J Acoust Soc Am 1994;95:530-41.
9. Mast TD, Hinkelman LM, Orr MJ, Waag RC. The effect of abdominal wall morphology on ultrasonic pulse distortion. Part II. Simulations. J Acoust Soc Am 1998;104:3651-64.
10. Hinkelman LM, Mast TD, Metlay LA, Waag RC. The effect of abdominal wall morphology on ultrasonic pulse distortion. Part I. Measurements. J Acoust Soc Am 1998;104:3635-49.
11. Hinkelman LM, Liu DL, Waag RC, Zhu Q, Steinberg BD. Measurement and correction of ultrasonic pulse distortion produced by the human breast. J Acoust Soc Am 1995;97:1958-69.
12. Hinkelman LM, Szabo TL, Waag RC. Measurements of ultrasonic pulse distortion produced by human chest wall. J Acoust Soc Am 1997;101:2365-73.
13. Finkelhor RS, Moallem M, Bahler RC. Characteristics and impact of obesity on the outpatient echocardiography laboratory. Am J Cardiol 2006;97:1082-4.
14. El Hajj MC, Litwin SE. Echocardiography in the Era of Obesity. J Am Soc Echocardiogr 2020;33:779-87.
15. Hirama M, Ikeda O, Sato T. Adaptive ultrasonic array imaging system through an inhomogeneous layer. J Acoust Soc Am 1982;71:100-9.
16. Flax SW, O'Donnell M. Phase-aberration correction using signals from point reflectors and diffuse scatterers: basic principles. IEEE Trans Ultrason Ferroelectr Freq Control 1988;35:758-67.
17. O'Donnell M, Flax SW. Phase-aberration correction using signals from point reflectors and diffuse scatterers: measurements. IEEE Trans Ultrason Ferroelectr Freq Control 1988;35:768-74.
18. Nock L, Trahey GE, Smith SW. Phase aberration correction in medical ultrasound using speckle brightness as a quality factor. J Acoust Soc Am 1989;85:1819-33.
19. Liu DL, Waag RC. Time-shift compensation of ultrasonic pulse focus degradation using least-mean-square error estimates of arrival time. J Acoust Soc Am 1994;95:542-55.
20. Prada C, Fink M. Selective focusing through inhomogeneous media: the DORT method. In: 1995 IEEE Ultrasonics Symposium. Proceedings. An International Symposium. IEEE, 1995;2:1449-53.
21. Berkhoff AP, Thijssen JM. Correction of concentrated and distributed aberrations in medical ultrasound imaging. In: 1996 IEEE Ultrasonics Symposium. Proceedings. IEEE, 1996;2:1405-10.
22. Krishnan S, Rigby KW, O'Donnell M. Efficient parallel adaptive aberration correction. IEEE Trans Ultrason Ferroelectr Freq Control 1998;45:691-703.
23. Måsøy SE, Angelsen B, Varslot T. Estimation of ultrasound wave aberration with signals from random scatterers. J Acoust Soc Am 2004;115:2998-3009.
24. Varslot T, Krogstad H, Mo E, Angelsen BA. Eigenfunction analysis of stochastic backscatter for characterization of acoustic aberration in medical ultrasound imaging. J Acoust Soc Am 2004;115:3068-76.
25. Waag RC, Astheimer JP. Statistical estimation of

ultrasonic propagation path parameters for aberration correction. IEEE Trans Ultrason Ferroelectr Freq Control 2005;52:851-69.

26. Herbert E, Pernot M, Montaldo G, Fink M, Tanter M. Energy-based adaptive focusing of waves: application to noninvasive aberration correction of ultrasonic wavefields. IEEE Trans Ultrason Ferroelectr Freq Control 2009;56:2388-99.

27. Osmanski BF, Montaldo G, Tanter M, Fink M. Aberration correction by time reversal of moving speckle noise. IEEE Trans Ultrason Ferroelectr Freq Control 2012;59:1575-83.

28. Lambert W, Cobus LA, Robin J, Fink M, Aubry A. Ultrasound Matrix Imaging—Part II: The Distortion Matrix for Aberration Correction Over Multiple Isoplanatic Patches. IEEE Trans Med Imaging 2022;41:3921-38.

29. Bendjador H, Deffieux T, Tanter M. SVD beamforming for ultrafast aberration correction and real-time speed-of-sound quantification. In: 2020 IEEE International Ultrasonics Symposium (IUS). IEEE, 2020:1-4.

30. Rigby KW, Chalek CL, Haider BH, Lewandowski RS, O'Donnell M, Smith LS, Wildes DG. Improved in vivo abdominal image quality using real-time estimation and correction of wavefront arrival time errors. In: 2000 IEEE Ultrasonics Symposium. Proceedings. An International Symposium (Cat. No. 00CH37121). IEEE, 2000;2:1645-53.

31. Østvik A, Smistad E, Aase SA, Haugen BO, Lovstakken L. Real-Time Standard View Classification in Transthoracic Echocardiography Using Convolutional Neural Networks. Ultrasound Med Biol 2019;45:374-84.

32. Mallart R, Fink M. Adaptive focusing in scattering media through sound-speed inhomogeneities: The van Cittert Zernike approach and focusing criterion. J Acoust Soc Am 1994;96:3721-32.

33. Hollman KW, Rigby KW, O'Donnell M. Coherence factor of speckle from a multi-row probe. In: 1999 IEEE Ultrasonics Symposium. Proceedings. International Symposium (Cat. No. 99CH37027). IEEE, 1999;2:1257-60.

34. Fatemi A, Berg EAR, Rodriguez-Molares A. Studying the Origin of Reverberation Clutter in Echocardiography: In Vitro Experiments and In Vivo Demonstrations. Ultrasound Med Biol 2019;45:1799-813.

35. Dahl JJ, McAleavey SA, Pinton GF, Soo MS, Trahey GE. Adaptive imaging on a diagnostic ultrasound scanner at quasi real-time rates. IEEE Trans Ultrason Ferroelectr Freq Control 2006;53:1832-43.

36. Måsøy SE, Varslot T, Angelsen B. Iteration of transmit-beam aberration correction in medical ultrasound imaging. J Acoust Soc Am 2005;117:450-61.